https://doi.org/10.22226/2410-3535-2022-4-469-474

Synthesis and dielectric properties, XPS spectroscopy study of high-entropy pyrochlore

K. N. Parshukova[†,1], N. A. Sekushin[2], B. A. Makeev[3], M. G. Krzhizhanovskaya[4], A. V. Koroleva[4], N. A. Zhuk[1]

[†]kristinaparshukova17@gmail.com

[1]Syktyvkar State University, Syktyvkar, 167001, Russia
[2]Institute of Chemistry of the Komi Science Center UB RAS, Syktyvkar, 167982, Russia
[3]Institute of Geology of the Komi Science Center UB RAS, Syktyvkar, 167982, Russia
[4]Saint Petersburg State University, St. Petersburg, 199034, Russia

It was established by XRD, that ceramics of the nominal composition $Bi_2Cr_{1/6}Mn_{1/6}Fe_{1/6}Co_{1/6}Ni_{1/6}Cu_{1/6}Ta_2O_{9+\Delta}$, regardless of the synthesis conditions, contained trace amounts of bismuth orthotantalate impurity. The phase-clean sample was obtained with a deficiency of bismuth atoms in the $Bi_{2-x}Cr_{1/6}Mn_{1/6}Fe_{1/6}Co_{1/6}Ni_{1/6}Cu_{1/6}Ta_2O_{9+\Delta}$ bismuth sublattice. The complex oxide crystallizes in the pyrochlore structural type (sp. gr. *Fd*-3*m*, a=10.4811(2) Å). Ceramics is characterized by a porous, loose microstructure with an average grain size of 0.5–1 μm. According to the XPS data, the transition element ions in pyrochlore are predominantly in the Cr (III), Fe (III), Mn (II), Co (II), Ni (II), Cu (II) states. At room temperature, the permittivity and dielectric loss tangent of $Bi_{2-1/3}Cr_{1/6}Mn_{1/6}Fe_{1/6}Co_{1/6}Ni_{1/6}Cu_{1/6}Ta_2O_{9+\Delta}$ are ≈46 and ≈0.004 at 1 MHz, respectively. An equivalent circuit is proposed that simulates the electrical properties of the sample.

Keywords: high-entropy oxides, pyrochlore, bismuth tantalate, doping with transitional 3d-elements, impedance spectroscopy, XPS spectroscopy.

1. Introduction

Bismuth-containing synthetic pyrochlores have useful properties that are in demand in the creation of multilayer ceramic capacitors, electronic devices and microwave filters. In addition to excellent dielectric properties (low dielectric losses and high dielectric constant, adjustable temperature coefficient of capacitance), pyrochlores exhibit catalytic properties in the UV and visible spectral regions [1–3]. The tolerance of the crystal structure of pyrochlore to the substitution of cations of both sublattices and oxygen vacancies makes it possible to significantly vary the chemical composition of pyrochlores and control their functional properties. Currently, pyrochlores based on bismuth tantalate are being actively studied [4–6]. It has been established that such pyrochlores have moderate dielectric properties compared to similar pyrochlores based on bismuth niobate. For example, for iron-containing pyrochlores $Bi_{3.36}Fe_{2.08+x}Ta_{2.56-x}O_{14.56-x}$ ($-0.32 \le x \le 0.48$), the values of the dielectric constant are ≈78–92 and the dielectric losses are relatively small ≈10^{-1} at 1 MHz [7]. Comparable dielectric properties are typical for $Bi_{3+5/2x}Mg_{2-x}Ta_{3-3/2x}O_{14-x}$ ($0.12 \le x \le 0.22$), and their dielectric constant varies from 70 to 85, and the dielectric loss tangent is 10^{-3} (1 MHz) [8]. Moreover, copper-containing bismuth tantalates exhibit a multiple permittivity at temperatures above room temperature [9,10]. A feature of these pyrochlores is the unfilled bismuth sublattice due to the presence of the $6s^2$ electron pair and the ability of transition element ions (Cu, Mn, Co) to simultaneously locate in the cationic sublattices of bismuth (A_2O') and tantalum (B_2O_6) [11]. Recently, high-entropy compounds containing five or more types of atoms in an equiatomic amount have attracted much attention. The disordered position of all atoms at the sites of the crystal lattice leads to an increased configurational entropy of such a phase, which is reflected in the name of this class of materials [12]. The synthesis of high-entropy compounds with perovskite, magniplumbite, and pyrochlore structures is described in [13–17]. Such compounds have unique mechanical properties — high strength and hardness. In addition, some of them exhibit the magnetocaloric effect and superconductivity. Other properties of high-entropy compounds are also being studied: tribological, transport (diffusion, electrical and thermal conductivity), and magnetic. These materials are promising as heat-resistant protective coatings and catalysts. In this work, we show the possibility of synthesizing multicomponent pyrochlores based on bismuth tantalate containing equimolar amounts of atoms of the 3d element. The samples have prospects for use as dielectric materials and catalysts, as well as elements of solar cells.

2. Experimental

High-entropy pyrochlore was synthesized by the standard ceramic technology from the corresponding Bi (III), Ta (V),

Ni (II), Co (II), Cu (II), Mn (III), Cr (III), Fe (III) oxides analytical grade. The stoichiometric mixture of precursors was finely ground and homogenized in a jasper mortar for one hour. The resulting homogeneous mixture was compacted in the form of disks using a Plexiglas mold. The samples were calcined in air in stages at a temperature of 650, 850, 950, 1050°C for 60 hours. At each stage, the samples were again ground and pressed into tablets.

X-ray phase analysis was performed using a Shimadzu 6000 X-ray diffractometer (CuK_α radiation; $2\theta = 10 - 60°$; scanning speed 2.0°/min). The unit-cell parameters were calculated at every temperature step by Pawley approach and the crystal structure of high-entropy pyrochlore was refined at 25°C by Rietveld method using the Topas 5.0 software package [18].

Surface morphology studies and local quantitative elemental analysis of the samples were performed using a scanning electron microscope (Tescan VEGA 3LMN) and an energy dispersive X-ray spectrometer (INCA Energy 450). In order to study electrical properties, metallic Ag electrodes were applied onto both sides of the ceramic discs and sintered at 650°C for 1 h. The measurements were carried out with an E7–28 impedancemeter (frequency range of $25 - 10^7$ Hz) at temperatures from 25 up to 450°C. XPS analysis was performed on a Thermo Scientific ESCALAB 250Xi X-ray spectrometer with AlK_α radiation (1486.6 eV). An ion-electronic charge compensation system was used to neutralize the sample charge. All peaks in the spectrum are calibrated relative to the C1s peak at 284.6 eV. The experimental data were processed using the ESCALAB 250 Xi software.

3. Results and discussion

According to the X-ray-phase analysis, a sample of the complex composition of $Bi_2Cr_{1/6}Mn_{1/6}Fe_{1/6}Co_{1/6}Ni_{1/6}Cu_{1/6}Ta_2O_{9+\Delta}$ is crystallized in the structural type of pyrochlore (sp. gr. *Fd*-3*m*) and, regardless of the conditions of the synthesis, contains an admixture orthotantalate of bismuth of the triclinic modification (β-$BiTaO_4$). Relying on our previous experience, we attempted to synthesize a bismuth-deficient composition in order to obtain a single-phase high-entropy preparation and study its properties. For this purpose, we additionally created vacancies in the bismuth sublattice by a value corresponding to the amount of impurity bismuth orthotantalate in the initial sample. The point is that in bismuth pyrochlores, the bismuth sublattice must remain vacant due to the stereoactive $6s^2$ electron pair. When doped with atoms of transition elements, most of the 3d ions are distributed into the tantalum (V) octahedral sublattice, creating oxygen vacancies and distorting the polyhedral environment, thereby causing stresses in the crystal structure as a whole. In order to relieve stresses in the crystal structure, some especially large 3d ions (Co (II), Mn (II), Cu (II)) compared to Ta (V) ions ($R(Ta^{5+})_{cn-6} = 0.064$ nm, $(R(Cu^{2+})_{cn-6} = 0.073$ nm, $R(Co^{2+})_{cn-6} = 0.0745$ nm, $R(Mn^{2+})_{cn-6} = 0.083$ nm) [19], are partially located in the position of bismuth (III), violating vacancy balance The system responds to this placement by creating vacancies in the bismuth sublattice by isolating the bismuth orthotantalate phase as an impurity [20]. Thus, the amount of bismuth orthotantalate impurity, in most cases, is equivalent to the amount of 3d ions located in the bismuth position. Guided by this idea, we made a bismuth-deficient composition $Bi_{2-x}Cr_{1/6}Mn_{1/6}Fe_{1/6}Co_{1/6}Ni_{1/6}Cu_{1/6}Ta_2O_{9+\Delta}$ and synthesized it without changing the synthesis conditions. As a result, a single-phase pyrochlore was obtained, the X-ray pattern of which is shown in Fig. S1 (supplementary material). The calculation of the unit cell parameter of pyrochlore showed the value $a = 10.4811(2)$ Å. It is interesting, to note that the bismuth ion deficiency index is $x = 1/3$, which formally corresponds to the total number of two types of 3d ions of different nature. In order to determine the nature of ions that could, due to the large ionic radius and polarization properties similar to those of Bi (III) ions, be placed in the bismuth position, we performed an XPS analysis of the ions that make up pyrochlore. Figure 1 shows an overview XPS spectrum of the sample, which shows the core and valence levels of all elements that make up the complex oxide $Bi_{2-x}Cr_{1/6}Mn_{1/6}Fe_{1/6}Co_{1/6}Ni_{1/6}Cu_{1/6}Ta_2O_{9+\Delta}$ in the energy range 0–1350 eV. The chemical composition of the sample was analyzed using metal spectra due to the fact that the Survey XPS spectrum contains a relatively intense C1s peak, which is due to natural surface contamination of the sample, which can make an indefinite contribution to the intensity of the O1s peak. The assignment of the observed components to the chemical states of the ions was carried out on the basis of the literature data. Figure 1 shows the XPS spectra of the Bi4f and Ta4f core levels, the energy position of which is most consistent with the Bi_2O_3 and Ta_2O_5 oxide phases. Based on this fact, it was concluded that bismuth and tantalum ions are in the Bi^{+3} and Ta^{+5} charge states [21]. When considering the spectra of tantalum and bismuth atoms, it should be noted that the shape of the peaks unambiguously indicates that all tantalum and bismuth atoms are in the same charge state (there is no splitting and distortion of the peaks).

Let us turn to the consideration of the XPS Mn2p spectra shown in Fig. 1. A comparison of the XPS 2p spectrum of manganese in pyrochlore with the spectra of MnO [22], Mn_2O_3 [23], and MnO_2 [24] oxides known from the literature shows that the spectrum of the complex oxide coincides in shape and energy position of the absorption bands (641 and 653 eV) with MnO spectrum (641 and 652 eV), on the basis of this, it was concluded that the manganese atoms in the composition of pyrochlore mainly have the Mn^{2+} charge state. The XPS spectrum of iron showed (Fig. 1) the maxima of the Fe2p core levels with a characteristic spin-orbit splitting into two components $2p_{1/2}$ and $2p_{3/2}$ with binding energies of ≈710 and ≈725 eV. When comparing the positions of the maxima for the core levels of Fe2p in the complex oxide and iron oxides [25], it turned out that the lines in the spectrum are in good agreement both in number and in the energy position of the main features with iron (III) oxide, which allows us to assume that the iron atoms are in the same charge state with an effective charge of +3. Let us move on to the consideration of the Co2p spectra presented in Fig. 1. It should be noted that the peak responsible for the binding energy of the $Ta4p_{1/2}$ level falls into this energy range, which somewhat complicates the perception of cobalt spectra. Nevertheless, when comparing the spectrum of pyrochlore with the spectra of Co_3O_4 with the main spectral features at ≈780 and ≈797 eV and cobalt oxide CoO known from the

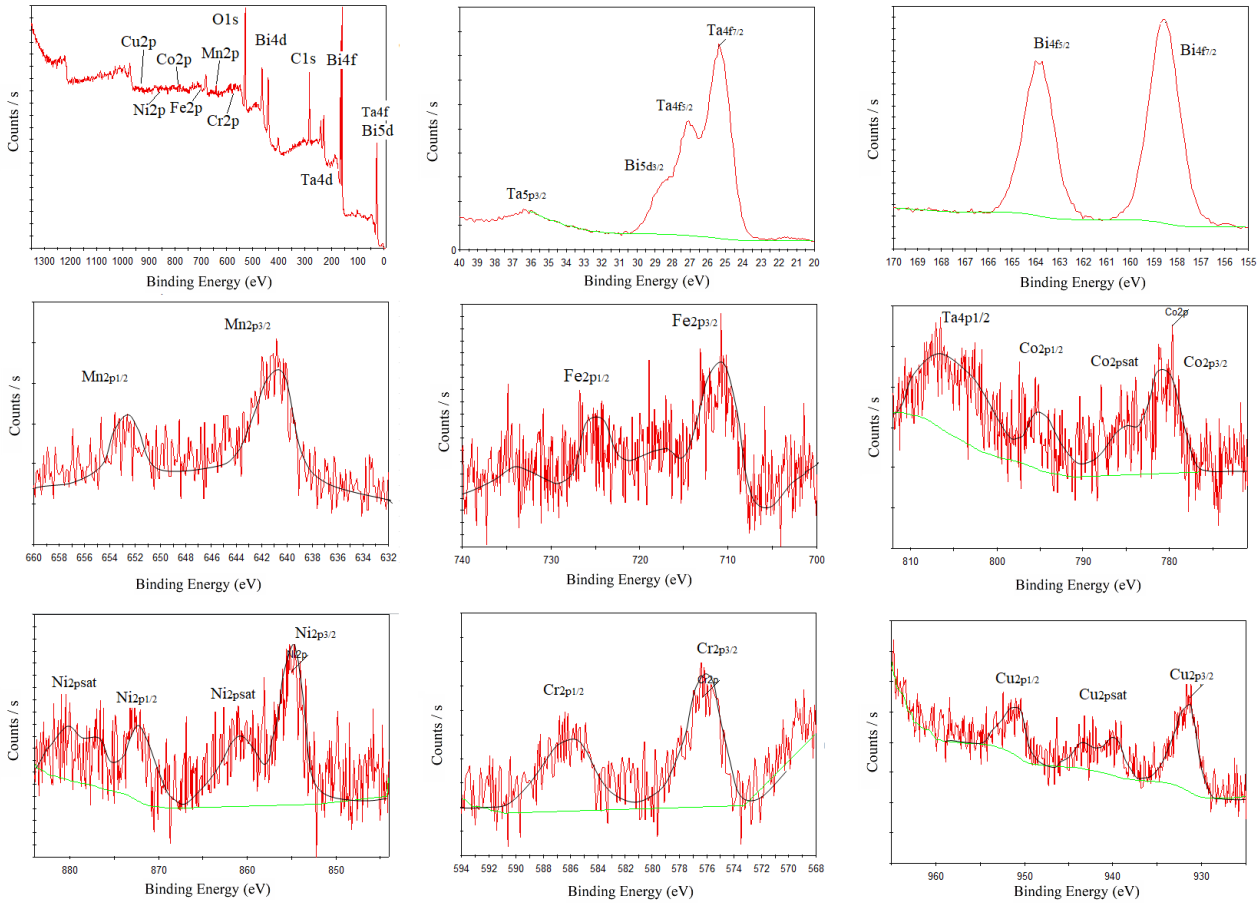

Fig. 1. (Color online) XPS survey spectrum, XPS Ta4f spectrum, XPS Bi4f spectrum, XPS Mn2p spectrum, XPS Fe2p spectrum, XPS Co2p spectrum, XPS Ni2p spectrum, XPS Cr2p spectrum, XPS Cu2p spectrum for $Bi_{2-1/3}Cr_{1/6}Mn_{1/6}Fe_{1/6}Co_{1/6}Ni_{1/6}Cu_{1/6}Ta_2O_{9+\Delta}$.

literature with binding energies of ≈781, ≈796 eV [26], one can see that the energy positions of the main peaks of the complex oxide almost coincides with the spectrum of CoO. In this case, the spectra of the sample and CoO contain pronounced satellite peaks (≈786 and 804 eV), which is a characteristic feature of almost all XPS 2p spectra of 3d atoms in the divalent state [27]. Based on these facts, it follows that the cobalt atoms in the sample under study are predominantly in the +2 charge state. The XPS spectrum of Ni2p shows two pronounced intense maxima with binding energies of 855 and 872 eV (Fig. 1). These energy values correspond to nickel (II) oxide, for which $Ni2p_{3/2}$ — 854 eV and $Ni2p_{1/2}$ — 872 eV. In this case, the spectra of the sample and NiO contain pronounced satellite peaks (861 and 880 eV), which is a characteristic feature of XPS 2p spectra of 3d atoms in the divalent state [27]. When comparing the spectra of the sample with the spectra of NiO obtained by us [4], it can be seen, as in all the cases considered above, that all nickel atoms are in the same charge state. The XPS Cr2p spectrum (Fig. 1) exhibits components of the Cr 2p levels — these are $2p_{1/2}$ and $2p_{3/2}$ with binding energies of ≈576 and ≈686 eV. Comparison of the spectrum of the complex oxide with the spectra of the oxides CrO_2, CrO_3, and Cr_2O_3 [28,29] shows that the spectrum of pyrochlore is close in terms of the energy position of the peaks to the spectrum of the oxide Cr_2O_3, which indicates that the chromium atoms in the composition of the complex oxide have a predominantly charge state of Cr^{+3}. Figure 1 shows the XPS spectrum of Cu2p core levels with singularities at 932 and 951 eV, the energy position of which is most consistent with copper (II) oxide, for which the corresponding binding energies are 934 and 954 eV [30]. Attention is drawn to the noticeable shift of the bands in the Cu2p spectrum of the sample, compared to CuO, to the low-energy region, which may be due to the presence of a certain fraction of Cu (I) ions in the sample (for Cu_2O — 932 and 951.5 eV [30]). Meanwhile, the Cu2p spectrum of pyrochlore clearly exhibits satellite lines (940 and 944 eV) characteristic of divalent Cu (II) ions [25]. In view of the foregoing, we can conclude that copper ions are predominantly in the Cu^{2+} charge state, while the presence of Cu (I) ions in a much smaller amount cannot be ruled out.

As the results of XPS spectroscopy show, 3d ions in the composition of multicomponent pyrochlore are predominantly in the states Cr (III), Fe (III), Mn (II), Co (II), Ni (II), Cu (II), of which, at least three types of ions — these are Mn (II), Co (II), Cu (II) have a radius significantly exceeding the ionic radius of tantalum (V) ($R(Ta^{5+})_{cn-6}$ = = 0.064 nm, $R(Ni^{2+})_{cn-6}$ = 0.069 nm, $R(Fe^{3+})_{cn-6}$ = 0.0645 nm, $R(Mn^{2+})_{cn-6}$ = 0.083 nm, $R(Cr^{3+})_{cn-6}$ = 0.0615 nm, $R(Cu^{2+})_{cn-6}$ = = 0.073 nm, $R(Co^{2+})_{cn-6}$ = 0.0745 nm). In this regard, one can expect their partial distribution in the bismuth position. On the basis of the study, it can be assumed that the distribution

of ions of transition 3d-elements in the cationic A-sites of pyrochlore is a consequence of the tension of the crystal structure as a result of doping with incommensurate ions. Local chemical analysis of the samples calcined at temperatures of 1000 and 1050°C by the EDS method showed that the sample calcined at 1050°C is characterized by a close composition to the given one. According to the results of EDS, it corresponds to the composition $Bi_{1.73}Cr_{0.18}Mn_{0.17}Fe_{0.16}Co_{0.2}Ni_{0.16}Cu_{0.26}Ta_2O_{9+\Delta}$, which differs little from the given composition, which is consistent with the conclusion of X-ray phase analysis about the single-phase nature of the samples. The ceramic microstructure is porous, reticulate, and consists of slightly melted randomly oriented elongated grains of small size 0.5–1 μm. In places, crystallites in the form of large agglomerates are observed on the ceramic surface.

For the $Bi_{2-1/3}Cr_{1/6}Mn_{1/6}Fe_{1/6}Co_{1/6}Ni_{1/6}Cu_{1/6}Ta_2O_{9+\Delta}$ sample, the dielectric permittivity and dielectric loss tangent in the frequency range from 25 Hz to 10 MHz, the change in the phase angle and the impedance modulus were estimated at room temperature (Fig. 2). At room temperature, the permittivity and dielectric loss tangent are ≈46 and ≈0.004 at 1 MHz, which is better than for single-phase $Bi_2NiTa_2O_9$ ($\varepsilon = 32$, $\tan\delta = 2\cdot10^{-3}$ at 1 MHz) [4], but worse than for $Bi_2FeTa_2O_{9.5}$ ($\varepsilon = 57$, $\tan\delta = 3\cdot10^{-3}$ at 1 MHz) [31]. An increase in the dielectric loss tangent can be associated with a decrease in the area of ceramic grain boundaries due to their partial fusion. As our latest studies have shown, for $Bi_{1.86}CoTa_2O_{9-\Delta}$ at room temperature and 1 MHz, the permittivity does not exceed 28, and the dielectric loss is ≈0.005. In the case of $Bi_2CrTa_2O_{9.5}$, the permittivity does not exceed ≈15 at RT, and the dielectric loss is ≈0.015 (at 1 MHz). In addition, the relaxation properties noted for copper-containing pyrochlores [16,17] do not manifest themselves in the studied temperature range. This suggests that the complex composition of ceramics levels out the features of each 3d component and its influence on the electrical properties. A general synergistic effect is manifested within the framework of the features of the crystal structure and the nature of the chemical elements that make up ceramics. In other words, ions of transition elements in the quantities they are present in pyrochlore (x=1/6, which is 8.3 percent of the total amount of tantalum ions) do not show their special nature, their individuality.

The electrical properties of ceramics in the temperature range 23–450°C are shown in Fig. S2 (supplementary material) and Figs. 3, 4.

The difference in the phase angle from 90 degrees and the manifestation of frequency-independent values of the impedance modulus with increasing temperature indicate a decrease in the resistance of the sample, which is due to the activation of ionic conductivity (Fig. S2, supplementary material). Hodographs have the shape of an almost perfect semicircle (Fig. 3). Therefore, the equivalent circuit of the sample is a parallel RC — two-terminal network.

The calculated parameters of the equivalent circuit are shown in Table S1 (supplementary material). It follows from Table S1 that two polarization mechanisms are present. The column 3 shows the values of the capacitance due to the electronic polarization of the bulk of the material. This capacitance is practically independent of temperature and frequency. The use of modeling makes it possible to separate this high-frequency capacitance (29 pF) from the low-frequency capacitance, which is probably caused by ionic processes at grain boundaries and pores. The high-frequency permittivity is 46–49. The dielectric losses of the high-frequency process are small. Taking them into account in the model by introducing a resistor in series with the capacitor does not improve the accuracy of the equivalent circuit.

The calculation of the activation energy showed values of 0.551±0.008 eV (Fig. 4), which does not exceed the values of activation energy for similar pyrochlores $Bi_{1.86}CoTa_2O_{9-\Delta}$ (0.58 eV) and $Bi_2CrTa_2O_{9.5}$ (0.78 eV). The through conductance was calculated from the R1 values (second column of Table 1, supplementary material). Figure 4 shows graphs of the average permittivity versus temperature. As the temperature rises, the ion migration polarization increases significantly. Thanks to the equivalent circuit, it was possible to separately investigate the ohmic (or Joule) losses, for which the resistor R1 is responsible, and the dielectric losses, which are modeled by the "R2-CPE" circuit. The loss tangent in this circuit can be calculated using the formula:

$$\tan\delta = \mathrm{ctg}\frac{\pi P}{2} + (\omega\tau)^P \sin^{-1}\frac{\pi P}{2}, \qquad (1)$$

where $\tau = (R_2\cdot T)^{1/P}$ — the environment parameter having the dimension of time.

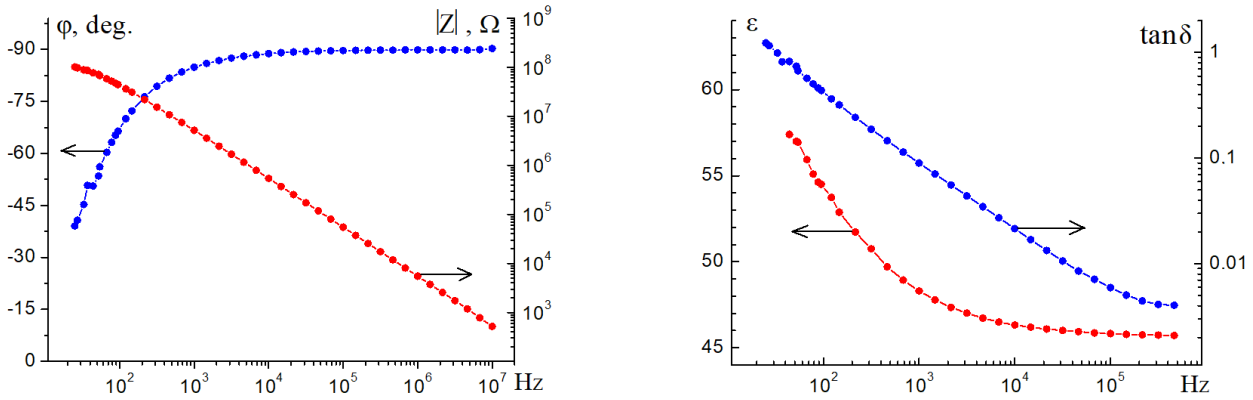

Fig. 2. (Color online) Frequency dependences of the modulus and phase of the impedance of the $Bi_{2-1/3}Cr_{1/6}Mn_{1/6}Fe_{1/6}Co_{1/6}Ni_{1/6}Cu_{1/6}Ta_2O_{9+\Delta}$ sample; frequency dependences of permittivity (ε) and dielectric loss tangent (tan δ) at 23°C.

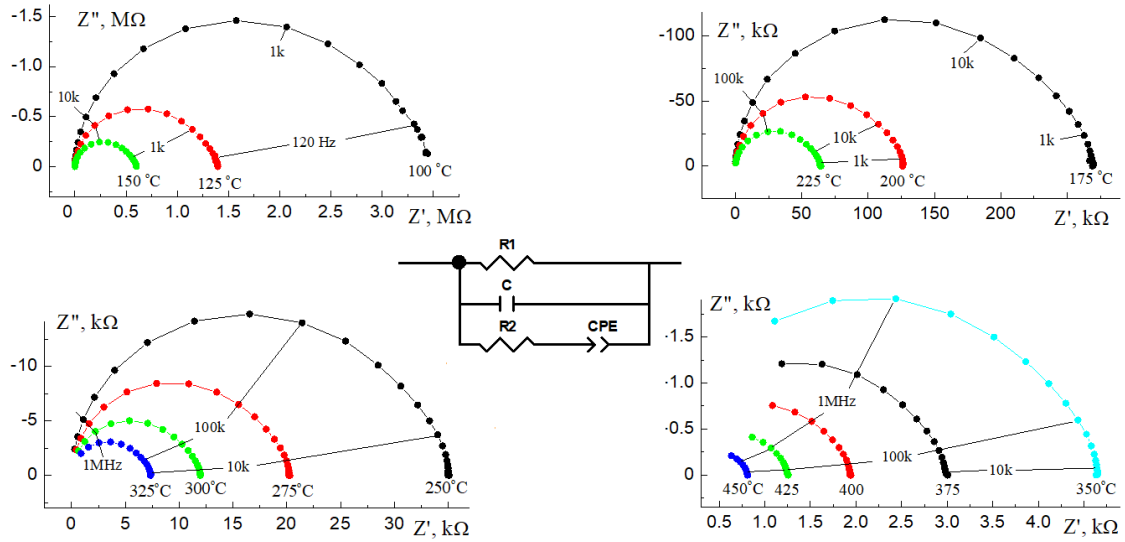

Fig. 3. (Color online) Hodographs of the $Bi_{2-1/3}Cr_{1/6}Mn_{1/6}Fe_{1/6}Co_{1/6}Ni_{1/6}Cu_{1/6}Ta_2O_{9+\Delta}$ sample in the temperature range 100 – 450°C.

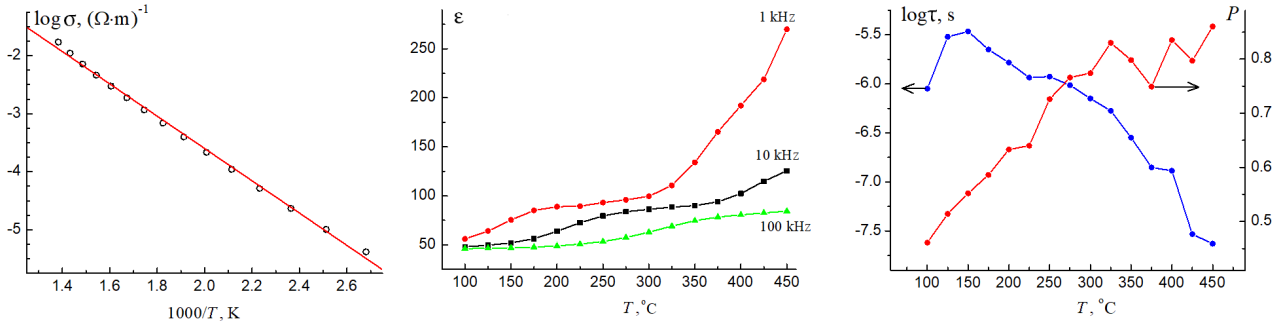

Fig. 4. (Color online) Temperature dependence of the through conductivity of $Bi_{2-1/3}Cr_{1/6}Mn_{1/6}Fe_{1/6}Co_{1/6}Ni_{1/6}Cu_{1/6}Ta_2O_{9+\Delta}$ on the Arrhenius scale; dielectric constant versus temperature at 1, 10 and 100 kHz; temperature dependences of material parameters τ and *P*.

It should be noted that the product $R_2 \cdot T$ does not depend (in the first approximation) on the geometric dimensions of the plane-parallel sample, but has an inconvenient dimension: "time *P*". At the same time, the parameter *P* also, if edge effects are not taken into account, does not depend on the dimensions of the plane-parallel sample. Therefore, τ and *P* are characteristics of an inhomogeneous dielectric or semiconductor medium. Figure 4 shows the dependences of these quantities on temperature. The parameter *P* characterizes the homogeneity of the medium. The closer it is to 1, the more homogeneous the environment. The parameter τ affects the dielectric losses, which follows from formula (1). It is also a characteristic of the rate of polarization of an inhomogeneous medium. Such an environment has one common property. The faster it polarizes, the lower the dielectric loss. Thus, as the temperature increases, the polarization of the medium proceeds faster. However, at a temperature of about 100°C, an increase in τ is observed, which can be explained by desorption from the surface of the water sample. When heated, the uniformity of polarization increases. The increase in noise is due to the fact that at high temperatures information is extracted only from a part of the hodograph, since most of it is outside the observation region.

4. Conclusions

High-entropy pyrochlore $Bi_{2-1/3}Cr_{1/6}Mn_{1/6}Fe_{1/6}Co_{1/6}Ni_{1/6}Cu_{1/6}Ta_2O_{9+\Delta}$ (sp. gr. *Fd*-3*m*, *a* =10.4811(2) Å) was synthesized by the solid-phase reaction method. Phase-clean pyrochlore was obtained at 1050°C. The microstructure of the sample is porous, loose, formed by partially intergrown grains with an average size of 0.5 – 1 μm. According to the X-ray spectroscopy data, the ions in the composition of pyrochlore are predominantly in the traditional ionic forms Cr (III), Fe (III), Mn (II), Co (II), Ni (II), Cu (II). The sample exhibits dielectric properties: the permittivity and dielectric loss tangent are ≈46 and ≈0.004 (*RT*, 1 MHz). It has been suggested that the complex composition of ceramics levels out the features of each 3d component and its influence on the electrical properties.

Supplementary material. *The online version of this paper contains supplementary material available free of charge at the journal's website (lettersonmaterials.com).*

Acknowledgements. The authors thank the X-ray Diffraction Center SPSU for providing instrumental and computational resources. The XPS studies were performed on the equipment of

the Resource Center "Physical methods of surface investigation" of the Scientific Park of St. Petersburg University.

References

1. S. Murugesan, M.N. Huda, Y. Yan, M.M. Al-Jassim, V. Subramanian. J. Phys. Chem. 114, 10598 (2010). Crossref
2. C.C. Khaw, K.B. Tan, C.K. Lee. Ceram. Intern. 35, 1473 (2009). Crossref
3. G. Giampaoli, T. Siritanon, B. Day, J. Li, M. A. Subramanian. Prog. Solid State Chem. 50, 16 (2018). Crossref
4. N.A. Zhuk, M.G. Krzhizhanovskaya, A.V. Koroleva, S.V. Nekipelov, V.V. Kharton, N.A. Sekushin. Inorgan. Chem. 60, 4924 (2021). Crossref
5. M.P. Chon, K.B. Tan, C.C. Khaw, Z. Zainal, Y.H. Taufiq-Yap, S.K. Chen, P.Y. Tan. J. Alloys Comp. 675, 116 (2016). Crossref
6. N.A. Zhuk, M.G. Krzhizhanovskaya. Ceram. Int. 47, 30099 (2021). Crossref
7. F.A. Jusoh, K.B. Tan, Z. Zainal, S.K. Chen, C.C. Khaw, O.J. Lee. J. Mater. Res. Techn. 9, 11022 (2020). Crossref
8. P.Y. Tan, K.B. Tan, C. Khaw, Z. Zainal, S.K. Chen, M.P. Chon. Ceram. Intern. 38, 5401 (2021). Crossref
9. N.A. Zhuk, M.G. Krzhizhanovskaya, A.V. Koroleva, N.A. Sekushin, S.V. Nekipelov, V.V. Kharton, B.A. Makeev, V.P. Lutoev, Y.D. Sennikova. Inorg. Chem. 61, 4270 (2022). Crossref
10. N.A. Zhuk, N.A. Sekushin, M.G. Krzhizhanovskaya, V.V. Kharton. Sol. St. Ion. 377, 115868 (2022). Crossref
11. M.A. Subramanian, G. Aravamudan, G.V. Subba Rao. Prog. Solid State Chem. 15, 55 (1983). Crossref
12. A.S. Rogachev. Physics of metals and metallology. 121, 807 (2020). Crossref https://doi.org/10.1134/S0031918X20080098
13. C.C. Khaw, K.B. Tan, C.K. Lee, A.R. West. J. Eur. Ceram. Soc. 32, 671 (2012). Crossref
14. G. Karthick, L. Raman, B.S. Murty. J. Mater. Sci. Technol. 82, 214 (2021). Crossref
15. H. Yang, G. Lin, H. Bu, H. Liu, L. Yang, W. Wang, X. Lin, C. Fu, Y. Wang, C. Zeng. Ceram. Int. 48, 6956 (2022). Crossref
16. D. Liu, Y. Wang, F. Zhou, B. Xu, B.Lv. Ceram. Int. 47, 29960 (2021). Crossref
17. D.A. Vinnik, E.A. Trofimov, V.E. Zhivulin, O.V. Zaitseva, S.A. Gudkova, A.Yu. Starikov, D.A. Zherebtsov, A.A. Kirsanova, M. Häßner, R. Niewa. Ceram. Intern. 45, 12942 (2019). Crossref
18. Bruker AXS. Topas 5.0. General profile and structure analysis software for powder diffraction data. Karlsruhe, Germany. 2014.
19. R.D. Shannon. Acta Crystallogr. A. 32, 751 (1976). Crossref
20. N.A. Zhuk, M.G. Krzhizhanovskaya, V.A. Belyy, V.V. Kharton, A.I. Chichineva. Chem. Mater. 32, 5493 (2020). Crossref
21. T.J. Regan, H. Ohldag, C. Stamm, F. Nolting, J. Luning, J. Stöhr, R.L. White. Phys. Rev. 64, 214422 (2001). Crossref
22. R. Grissa, H. Martinez, S. Cotte, J. Galipaud, B. Pecquenard, F.L. Cras. Applied Surface Science. 411, 449 (2017). Crossref
23. M.A. Stranick. Mn_2O_3 by XPS. Surface Science Spectra. 6, 39 (1999). Crossref
24. F. Gri, L. Bigiani, A. Gasparotto, C. Maccato, D. Barreca. Surface Science Spectra. 25, 024004 (2018). Crossref
25. J.F. Moulder. Handbook of X-ray Photoelectron Spectroscopy: A Reference Book of Standard Spectra for Identification and Interpretation of XPS Data. Physical Electronics Division, Perkin-Elmer Corporation (1992) 261 p.
26. M. Hassel, H.-J. Freund. Surface Science Spectra. 4, 273 (1996). Crossref
27. D.D. Sarma, C.N.R. Rao. J. Electron Spectrosc. Relat. Phenom. 20, 25 (1980). Crossref
28. H.A. Bullen, S.J. Garrett. Single Crystal Surfaces. Surface Science Spectra. 8, 225 (2001). Crossref
29. S.-Y. Jeong, J.-B. Lee, H. Na, T.-Y. Seong. Thin Solid Films. 518, 4813 (2010). Crossref
30. D. Barreca, A. Gasparotto, E. Tondello. Surface Science Spectra. 14, 41 (2007). Crossref
31. N.A. Zhuk, N.A. Sekushin, V.G. Semenov, A.V. Fedorova, A.A. Selyutin, M.G. Krzhizhanovskaya, V.P. Lutoev, B.A. Makeev, V.V. Kharton, D.N. Sivkov, A.D. Shpynova. J. Alloys Comps. 903, 163928 (2022). Crossref